Nano Today 58 (2024) 102465

Contents lists available at ScienceDirect

Nano Today

journal homepage: www.elsevier.com/locate/nanotoday

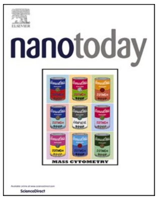

A multichannel nucleic acid-based Ca^{2+} nanomodulator induces multilevel destruction of mitochondria for cancer therapy

Weifang Gong [a], Tingting Zhao [a], He Yuan [a], Geng Yang [a], Weicai Wang [a], Xuemei Li [a,*], Huangxian Ju [b,*]

[a] Key Laboratory of Detection Technology for Tumor Makers School of Chemistry and Chemical Engineering, Linyi University, Linyi 276005, PR China
[b] State Key Laboratory of Analytical Chemistry for Life Science, School of Chemistry and Chemical Engineering, Nanjing University, Nanjing 210023, PR China

ARTICLE INFO

Key words:
Nucleic acid-based Ca^{2+} nanomodulator
Curcumin
Mitochondrial Ca^{2+} overload
Mitochondrial biomineralization
Cancer therapy

ABSTRACT

Mitochondria play a crucial function in tumor proliferation and apoptosis, and inducing mitochondrial dysfunction in cells has emerged as a promising therapeutic approach for tumors. Here, curcumin (CUR) is enrolled in amorphous calcium phosphate (ACP) through the coprecipitation method, followed by Cy5.5-labeled DNA was adsorbed on its surface to propose an acidity-responsive nucleic acid-based nanomodulator (ACP@C-D) to enhance Ca^{2+} overload and mitochondrial biomineralization for cancer therapy by amplifying intra-mitochondrial Ca^{2+} concentration. After tumor cell administration, the ACP@C-D will disintegrate in the acidic environment to enhance Ca^{2+} overload by the combined interaction of a dramatic increase in Ca^{2+} concentration and Ca^{2+} efflux inhibition by Cur. Moreover, the mitochondrial targeting ability of Cy5.5 allows DNA enrichment at mitochondrial, and the phosphate on DNA provides reaction sites for Ca^{2+} to achieve mitochondrial biomineralization thus mitochondrial dysfunction, which is reported for the first time. The facile and functional strategy of the nanomodulator will provide new insights into inmitochondria-based cancer therapy.

Introduction

Effective treatment of cancer is an urgent challenge to address, which can save millions of people's lives [1,2]. In recent years, researchers have developed many therapeutic modalities for cancer treatment, such as photothermal therapy, photodynamic therapy, immunotherapy, etc [3–6]. Although certain results have been achieved, there are still some sturdy challenges that limit their application, limited oxygen concentration, insufficient near-infrared penetration, and cellular multidrug resistance [7–9]. Mitochondria, the "energy factory" of cells, provide energy for normal cellular life activities [10]. Apart from supplying energy to cells, mitochondria are involved in processes such as apoptosis, cellular messaging and cellular differentiation, and possess the ability to regulate cell growth and cell cycle [11,12]. It has been shown that abnormalities in mitochondrial metabolism and mitochondrial function are associated with tumor cell proliferation and metastasis [13]. Therapies targeting disruption of mitochondrial function are emerging as an attractive anti-cancer strategy [14–16].

Ca^{2+}, as the most important second messenger, is involved in the regulation of various physiological processes and is closely related to biological signaling [17]. However, when intracellular Ca^{2+} homeostasis is disrupted, aberrant Ca^{2+} overload will trigger a range of mitochondrial disorders, including reduced mitochondrial membrane potential (MMP), decreased adenosine triphosphate (ATP) levels and activation of mitochondria-mediated apoptotic pathways [18–20]. Recently, anticancer therapy based on Ca^{2+} overload has gained increasing attention. However certain concentration of intracellular Ca^{2+} limits the therapeutic effect of Ca^{2+} overload [21,22]. Therefore, effectively increasing the intracellular Ca^{2+} concentration becomes a key factor in enhancing Ca^{2+} overload [23,24]. Currently, there are two primary approaches to increasing intracellular Ca^{2+} concentration: the first is to deliver exogenous Ca^{2+} into the cell, and the second is to block the exocytosis of intracellular Ca^{2+}[25,26]. However, a single regulation has a limited effect on the improvement of Ca^{2+} overload, while significant improvement can be achieved by simultaneously realizing the combination of two regulations [27,28].

Ca^{2+}-based biomineralization is considered a highly biologically safe cancer treatment strategy [29]. This strategy usually utilizes chelating

---

* Corresponding authors.
E-mail addresses: xuemei_li@yeah.net (X. Li), hxju@nju.edu.cn (H. Ju).

https://doi.org/10.1016/j.nantod.2024.102465
Received 27 May 2024; Received in revised form 25 July 2024; Accepted 22 August 2024

agents to collect free Ca^{2+}, which further forms a calcified layer on the surface/ organelles of the tumor cells through mineralization to block their normal function, thereby inhibiting cell growth and proliferation [30–34]. Ca^{2+}-rich mitochondria within tumors are desirable candidates for mineralization, but slow induction of calcium chelators [35–38], insufficient targeting, and uncontrollable calcification processes remain a challenge at present. It has been reported that nucleic acids are excellent Ca^{2+} chelators, and the phosphate groups in nucleic acids can provide effective and sufficient reaction sites for Ca^{2+} mineralization [39–41]. However, its application in living cells has not been reported. Therefore, we decided to combine nucleic acids with calcium-based nanocarriers to investigate whether they can effectively achieve biomineralization in living cells.

Herein, a nucleic acid-based Ca^{2+} nanomodulator (ACP@C-D) was constructed to disrupt mitochondrial function in multiple ways for cancer therapy. As depicted in Scheme 1., curcumin (CUR), a calcium ion efflux inhibitor, was loaded into amorphous calcium phosphate (ACP) by co-precipitation and subsequently adsorbed cy5.5-labeled DNA aptamers onto its surface. The resultant ACP@C-D can be used in dual pathways to facilitate mitochondrial dysfunction-mediated cancer therapy and has been demonstrated with the following advantages: (1) ACP@C-D is facilitated by easy synthesis for efficient drug loading. (2) ACP@C-D can disintegrate at the TME and release CUR and Ca^{2+}, which can improve the accuracy of treatment. (3) Bursting increase in Ca^{2+} can effectively enhance Ca^{2+} overload. (4) The released CUR not only blocked the efflux of Ca^{2+} but also facilitated the flow of Ca^{2+} from the endoplasmic reticulum to the mitochondria, which can further amplify Ca^{2+} overload. (5) Mitochondrial targeting of Cy5.5 enriches DNA aptamers in mitochondria and provides sufficient and efficient chelation sites for Ca^{2+} to achieve mitochondrial biomineralization. (6) all the components of the constructed nanomodulators are biodegradable and bioabsorbable materials, which makes good biosafety. Altogether, the nanomodulator is reported as a promising nanomedicine that can provide a valuable reference for mitochondria-based tumor therapy.

Materials and methods

Materials

Cy5.5-DNA (5′-GCG GAC GAC CTG GGT GCT TGC TCA CGG TGT CGG GAG GCG G -Cy5.5–3′) sequences were purchased from Bioengineering (Shanghai, China). Calcium nitrate tetrahydrate ($Ca(NO_3)_2 \cdot 4H_2O$) was purchased from Xilong Science (Guangdong, China); diammonium phosphate ($(NH_4)_2HPO_4$), HEPES buffer (pH 7.6), sodium hydroxide (NaOH) were purchased from Maclean's (Shanghai, China); curcumin (CUR)was purchased from J&K Chemicals (Shanghai, China); mitochondrial dyes MitoTracker Green, Calcium Assay Kit (Methylmovanillin Blue Colorimetric Assay), Agarose was purchased from Shanghai Yuan Ye Biotechnology Co. (Shanghai, China); MTT toxicity assay kit was purchased from Prilosec (Beijing, China); V-FITC/PI apoptosis kit was purchased from Lianke Bio (Hangzhou, China). DNA strand was purchased from Bioengineering (Shanghai, China). The cell

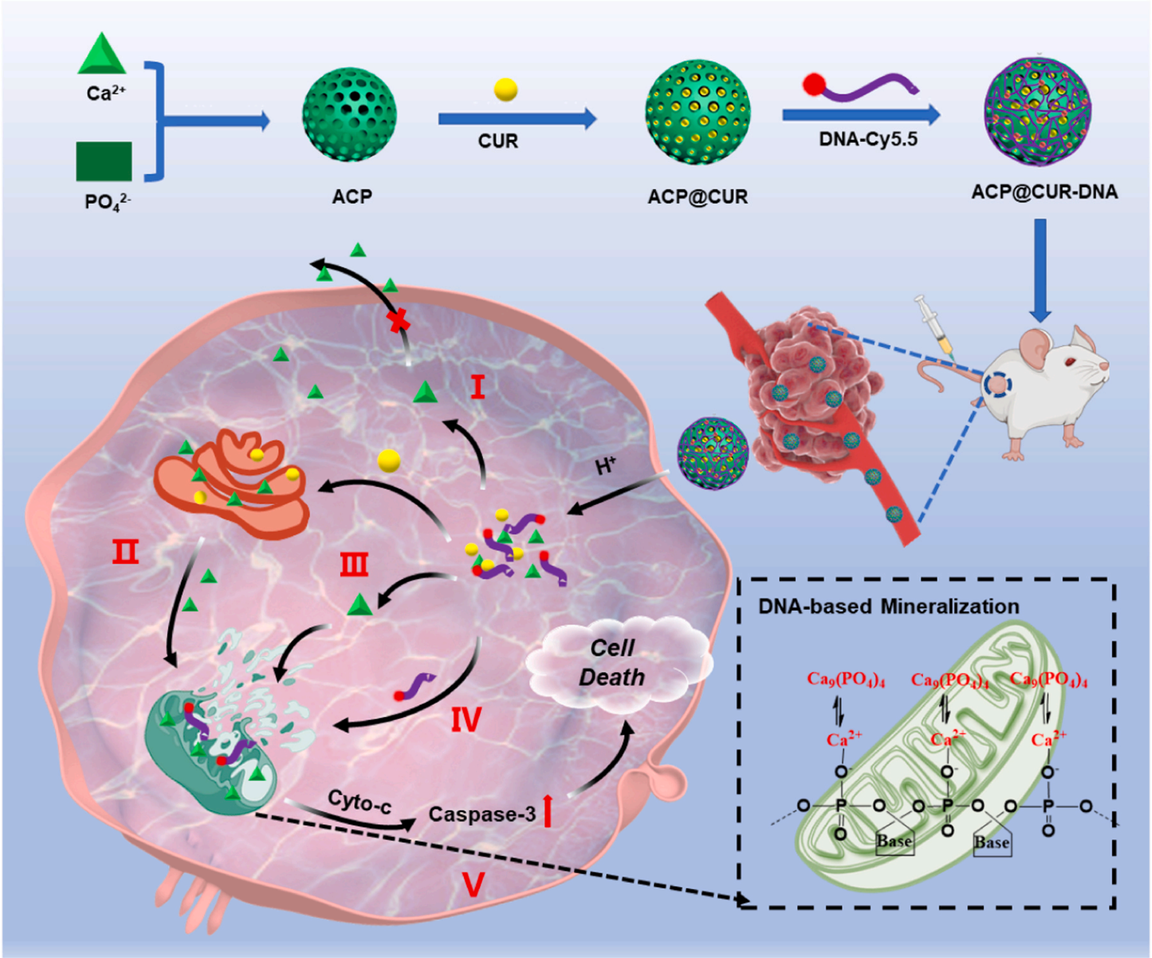

Scheme 1. Schematic illustration of the formation and the therapeutic mechanism of ACP@CUR-DAN (ACP@C-D) to inflict mitochondrial dysfunction for ferroptosis-based therapy. **I**, Ca^{2+} efflux inhibition; **II**, Endoplasmic reticulum Ca^{2+} release; **III**, Ca^{2+} flow to mitochondria; **IV**, Cy5.5-DNA target mitochondria; **V**, Nucleic acid as a template for the apoptotic mechanism of mitochondrial biomineralization.

line of 4T1 was obtained from the American Type Culture Collection (ATCC).

Synthesis of ACP@CUR-DNA (ACP@C-D)

Synthesis of amorphous calcium phosphate (ACP). ACP nanoparticles were prepared by co-precipitation method using $Ca(NO_3)_2 \cdot 4\ H_2O$ as calcium source and $(NH_4)_2HPO_4$ as phosphorus source[42]. Firstly, $Ca(NO_3)_2 \cdot 4\ H_2O$ was dissolved in 29 mL deionized water to form 1 mM aqueous solution. and then 29 mL of $(NH_4)_2HPO_4$ solution was added dropwise to the above solution, and the pH was adjusted to 8 with 1 M NaOH solution to keep the Ca/P molar ratio at 1.5. After that, the resulting suspension was stirred at 30 ℃ for 10 min. The suspension was then stirred at 30 ℃ for 10 min and aged at room temperature for 12 h. The precipitate was collected and washed with deionized water three times. The precipitate was dried under vacuum at room temperature to obtain a white powder.

Drug loading and release studies. CUR (5 mg/mL) was added to $Ca(NO_3)_2 \cdot 4\ H_2O$ solution and stirred at room temperature for 1 h. Then $(NH_4)_2HPO_4$ solution was slowly added to the above solution, and after gently stirred for 15 min at 30 ℃ in a water bath, the suspension was centrifuged at high speed (12,000 rpm, 20 min) to collect ACP@CUR (ACP@C). The absorbance of the supernatant at 424 nm was measured by the UV-Vis spectrophotometer method and the drug concentration in the supernatant was quantified according to the linear standard curve to calculate the drug loading (LC %). To assess the in vitro release of CUR, ACP@C was subjected to different pH (5.4, 7.4) (1 mL, 2 mg/mL), and 25 µl samples were aspirated at given time intervals and used in a calcium assay kit for analysis.

Synthesis of ACP@C-D. According to literature support, 50 µg/mL ACP adsorbs ~188 nM DNA aptamer. The fluorescence of Cy5.5-labeled DNA (200 nM) was measured in 10 mM HEPES buffer (pH 7.6) before the addition of ACP. Then 50 µg/mL ACP was added, incubated with Cy5.5-DNA for 1 h, centrifuged (5000 rpm,10 min), and the fluorescence intensity of the supernatant was measured. The amount of DNA adsorbed was calculated based on the attenuated fluorescence signal.

Characterizations

Transmission electron microscope (TEM-2100EX), fluorescence spectrophotometer (F-4600, Hitachi), UV spectrophotometer (Cary60), nano-potentiometric particle size analyzer (NaNo-ZS90, Malvern), enzyme labeling instrument (Epoch 2, BioTek, USA), flow cytometer (CutoFLEX, BackCoulter, USA), laser confocal scanning microscope (Leica TCS SP8), small animal 3D modal imaging system (IVIS SpectrumCT, PerkinElf). BackCoulter, USA), Laser Confocal Scanning Microscope (Leica TCS SP8), Small Animal 3D Multi-Modal Imaging System (IVIS SpectrumCT, PerkinElmer, USA), etc.

Cellular uptake behaviors of ACP@C-D

4T1 cells were inoculated at a density of 1×10^5 per well and cultured on laser confocal specialized dishes overnight. ACP@C-D (200 µg/mL) was added and co-incubated with the cells for 4 h. The cells were stained with Hoechest 33342 for 20 min and then with Mito Tracker Green for 30 min before being washed three times with PBS and observed by CLSM. Cellular uptake of ACP@C-D was also measured by flow cytometry.

In vitro cytotoxicity studies

Cytotoxicity was determined by MTT assay. Twenty thousand 4T1 cells and L02 cells were cultured overnight in 96-well plates. Different groups of drugs with the same drug concentration (200 ug/mL), different concentration gradients (25, 50, 100, 150, 200 ug/mL) of the same drug, and time gradients (12, 24 h) of different groups of drugs were analyzed, respectively. Subsequently, 10 µL of MTT Stock was added to each well at every 100 µL of the medium, and incubation was continued at 37 °C incubator for 4 h. After removing the medium, 100 µL of DMEM was added to each well, and incubated for 10 min at room temperature with slight shaking, and the absorbance at 570 nm was measured by enzyme marker.

In addition, apoptosis was analyzed by flow cytometry. Cells were incubated with different drug concentrations for 8 h. Cells were collected and analyzed by flow cytometry using Annexin V - FITC/PI Apoptosis Detection Kit.

In vivo biodistribution analysis

Inspired by the superior in vitro targeting ability, we further investigated the in vivo tumor targeting ability of ACP@C-D. We investigated the tumor-targeting ability of ACP@C-D in vivo using 4T1 tumor-bearing mice as a model. with Cy5.5 as a fluorescent imaging agent, to observe the biodistribution and tumor accumulation in 4T1 tumor-bearing mice. Fluorescence scans were performed using a small animal 3D multimodal imaging system (IVIS SpectrumCT, PerkinElmer) at different times (2, 4, 8, 12, 24, and 48 h) after intravenous injection. Meanwhile, major organs including the liver, spleen, kidney, heart, lung and tumor were sectioned for ex vivo imaging.

In vivo tumor model

The Army Medical University's Laboratory Animal Welfare and Ethics Committee approved all animal research carried out herein (Approval Number: AMUWEC20232924). All animal was obtained from Beijing Vital River Laboratory Animal Technology Co., Ltd. Firstly, the tumor mouse model was constructed. The 4T1 subcutaneous tumor model was established by subcutaneously injecting 1×10^6 4T1 cells in 100 µL of physiological saline into the right abdomen of 4–6-week-old BALB/c female mice. When the tumors reached approximately 100 mm3, the mice were randomly divided into five groups (n=4). During imaging experiments, mice were anesthetized with 2.5 % isoflurane in air at a flow rate of 0.3 L/min.

In vivo biodistribution analysis

Inspired by the superior in vitro targeting ability, we further investigated the in vivo tumor targeting ability of ACP@C-D. We investigated the tumor targeting ability of ACP@C-D in vivo using 4T1 tumor-bearing mice as a model, with Cy5.5 as a fluorescent imaging agent, to observe the biodistribution and tumor accumulation in 4T1 tumor-bearing mice. Fluorescence scans were performed using a small animal 3D multimodal imaging system (IVIS SpectrumCT, PerkinElmer) at different times (2, 4, 8, 12, 24 and 48 h) after intravenous injection. Meanwhile, major organs including liver, spleen, kidney, heart, lung and tumor were sectioned for ex vivo imaging.

In vivo antitumor efficacy

BALB/c mice carrying 4T1 tumors were divided into five groups, including (1) control group; (2) ACP group; (3) ACP-D group; (4) ACP@C group; and (5) ACP@C-D group. The treatment was performed separately through the tail vein, and the injection dose and frequency of injection were consistent in each group. Tumor size and body weight were measured daily (tumor volume $W^2 \times L/2$, W = width, L=length), and the relative tumor volume of each mouse was calculated as V/V_0 (V_0 was the tumor volume at the beginning of treatment). At the end of the experiment, the mice were executed, the tumors were stripped, the tissues were dissected, and the tumors and tissues were fixed with tissue fixative.

Statistical analysis

Each experiment was performed at least three times. All of the data were expressed as the mean ± standard deviation (SD) using GraphPad Prism software (version 8.2.1). Statistical analyses were performed using the Student's *t*-test. Significant differences between groups were considered at a minimum value of $p < 0.05$.

Results and discussion

Synthesis and characterization of ACP@C-D

ACP@C was obtained by the co-precipitation method, the TEM result (Fig. 1**A**) showed that the average size of ACP@C is ~70 nm, the EDS pattern revealed that there are strong correlations of Ca element, P

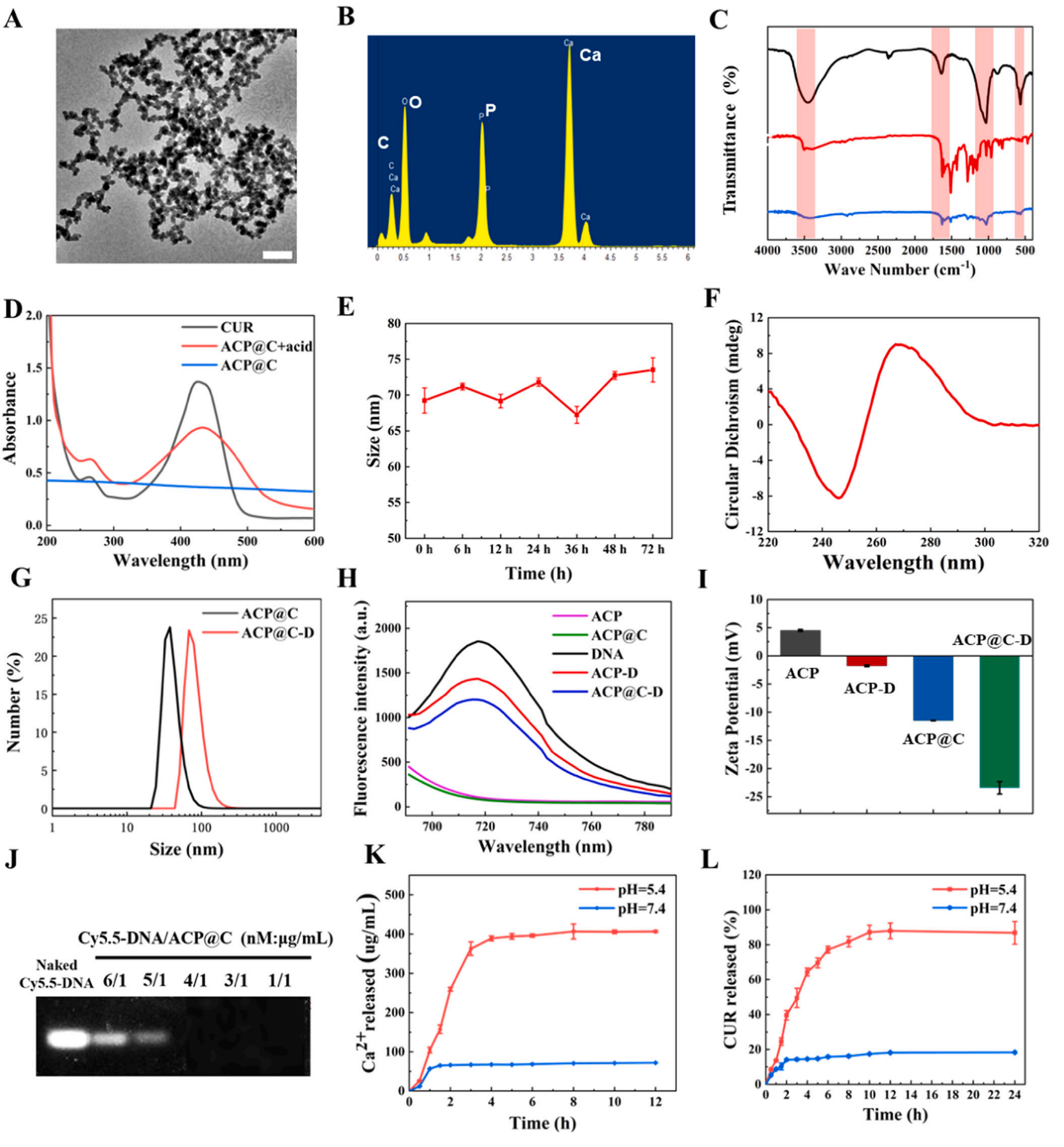

Fig. 1. Characterization of the nano platform. (**A**) TEM image of ACP@C (Scale bar=200 nm). **(B)** EDS spectrum of ACP@C. **(C)** FT-IR spectra of ACP, CUR, and ACP@C. **(D)** UV–vis absorption spectra of CUR, ACP@C and ACP@C+acid. **(E)** DLS analysis of the size of ACP during 72 h of incubation in PBS. **(F)** Circular dichroism spectra of Cy5.5-DNA (5 μM). **(G)** The hydrodynamic size of ACP@C and ACP@C-D. **(H)** Fluorescence spectra of ACP, DNA, ACP-D, ACP@C and ACP@C-D. **(I)** The surface charge of ACP, ACP-D, ACP@C and ACP@C-D. **(J)** Condensation ability and mass ratio of Cy5.5-DNA to ACP (nM:μg/mL) were determined by agarose gel electrophoresis. Ca^{2+}. (**K**) and CUR (**L**) release profiles at different pH values. The data are presented as the mean ±SD, n=3.

element, C element, and O element in ACP@C (Fig. 1**B**), which is consistent with the elemental composition of ACP and CUR. The successful synthesis of ACP@C was examined additionally by FT-IR spectra (Fig. 1**C**), the absorption peaks at 563 and 1033 cm^{-1} belonged to PO_4^{3-}, which indicated that the sample was calcium phosphate, and the unsplit peak at 563 cm^{-1} indicated the amorphous phase. ACP as a mesoporous material greatly improves drug loading capacity. We determined the specific surface area and pore size of ACP nanoparticles using a nitrogen physisorbent instrument, which resulted in a specific surface area of about 30.433 m^2/g, a total pore volume of about 0.1354 cm^3/g, and an average pore size of about 8.8 nm (Figure S1). Additionally, the absorption peak in the range of 850–1250 cm^{-1}, which can be assigned to the O-O and C-O modes of O-O-C (peroxide) from pure CUR. Besides, Zeta potential showed a change in the potential of ACP from positive to negative after loading CUR (Fig. 1**I**). according to the UV–vis spectrometer (Fig. 1**D**), The loading efficiency (LE) of the CUR was calculated to be 69.35 % based on the standard curve of the CUR and the change in the peak UV value before and after loading (Figure S2). For further biomedical applications, the storage stability of ACP@C-D was detected (Fig. 1**E**), there were no significant changes in size and zeta potential after 72 h of storage in PBS.

Reports have shown that DNA aptamers can act as chelators of Ca^{2+}, which is mainly characterized by the formation of tetrahedral structures. G-quadruplexes bind and interact closely with divalent cations such as calcium, strontium, and lead [43–45]· As shown in Fig. 1F, Circular dichroism (CD) spectroscopy shows positive bands around 260 nm as well as negative bands around 240 nm attributed to the G-quadruplex structure of the DNA aptamer we chose, a peak characteristic of parallel G-quadruplexes of DNA molecules. ACP has been extensively studied as an excellent nucleic acid delivery system due to its high affinity for the phosphate backbone. On this basis, Cy5.5-labeled DNA was adsorbed on the surface of ACP@C through to construct a nanomodulator (ACP@C-D). DLS results (Fig. 1**G**) revealed an increase in particle size (~100 nm) after loading DNA, as confirmed by their Zeta potential (Fig. 1**I**) and the TEM result (Figure S3). The fluorescence detection results (Fig. 1**H**) showed a significant enhancement of fluorescence in ACP@C-D compared to ACP@C. Additionally, the optimal mass ratio (nM:μg/mL) of DNA to ACP@C was measured by agarose gel electrophoresis (Fig. 1**J**), DNA was almost completely adsorbed by D/CP when the ratio is 200:50 (nM:μg/mL). And the LE of DNA was calculated as 84.6 % (Figure S4). The above results demonstrate that ACP@C-D has been successfully prepared with excellent stability.

ACP was also severed as a smart multicargo carrier for pH-responsive release and sustained release of a drug. We first explored the pH response degradation of ACP@C. As can be seen in Fig. 1**D,** the apparent absorption peak of CUR can be detected with the addition of acid. In addition, the impact of acid on the ACP@C was explored using TEM (Figure S5). ACP@C showed slight degradation after 1 h in an acidic buffer, significant fragmentation and decomposition were observed after 4 h. Following this, the release profiles of CUR and Ca^{2+} were examined at set time intervals and different pH conditions. As results showed in Fig. 1**L**, only a small amount of CUR could be detected after 12 h incubation at pH 7.4 and the cumulative release was about 18.7 %, while a burst CUR release was detected at pH 5.4 and the release amount of CUR can achieve to 89.4 %. Furthermore, the release profile of Ca^{2+} was found to be comparable to that of CUR (Fig. 1**K**), the concentration of Ca^{2+} in buffer can achieve 400 μg/mL after being immersed in pH 5.4 buffer within 12 h. Reasonably, ACP@C can improve the precision and safety of the therapeutic because of the acidic environments of tumors, which revealed the potential of ACP@C applied for tumor calcium mediated mitochondrial dysfunction.

Internalization and cytotoxicity study

Effective internalization of nanoparticles by tumor cells is a guarantee of therapeutic efficacy [46,47]. We explored cellular uptake of nanomodulator and mitochondrial targeting of Cy5.5-labeled DNA in 4T1 cells by confocal laser scanning microscopy (CLSM) and flow cytometry. As shown in Fig. 2 **A and B** , and quantifying their fluorescence intensity (Figure S6**)**, the red fluorescence of Cy5.5 gradually enhanced with increasing incubation time, suggesting a time-dependent cellular uptake behavior, more than sufficient to ensure a satisfactory therapeutic effect. Noteworthy, an increasing number of red/yellow puncta were noted as the incubation time increased, implying that DNA aptamers were gradually enriched in mitochondria. The results of flow cytometry also demonstrated the time-dependent fluorescence enhancement (Fig. 2 **C)**. Next, we wanted to learn whether nanomodulators could accurately achieve therapeutics at target cells. breast cancer cells 4T1 and normal cells L02 were co-incubated with nanomodulators at the same time. CLSM (Fig. 2**B**) and flow cytometry (Figure S7) results showed that an intense fluorescent signal can be observed in 4T1 cells, whereas it was barely observed in L02 cells. These results demonstrated that nanomodulators can achieve effective degradation in tumor cells but fail to do this in normal cells, further validating the therapeutic safety of nanomodulators.

To gain an insight into the cytotoxicity profiles of ACP@C-D, the in vitro Cell viability was tested in 4T1 cells and L02 cells through MTT assay. No significant cytotoxicity can be detected on L02 cells (Fig. 2**D**) was detected even the concentrations up to 200 μg/mL, meaning the excellent biosafety and low toxicity of ACP@C-D. After co-incubation with 4T1 cells, the relative cell viability of ACP-D and ACP@C groups was 69.3 % and 51.9 % respectively, indicating limited tumor killing ability of the single pathway regulated (Fig. 2**E**). By contrast, ACP@C resulted in a more severe tumor cell destruction as evidenced by a cell survival rate of 30.3 %, which may be due to the enhancement effect on mitochondrial dysfunction by the synergistic of Ca^{2+} overload and DNA-mediated mitochondrial mineralization. The therapeutic effects were further identified by quantitative flow cytometric analysis (Fig. 2 **F**). ACP@C-D resulted in a significant 4T1 cell necrosis (≈66.5 %) while only about 45.6 % and 30.0 % of cell necrosis could be observed in the ACP@C group and ACP-D group, respectively. In summary, ACP@C-D will open exciting opportunities for facilitating mitochondria-mediated cancer therapy thanks to its most efficient tumor killing ability.

ACP@C-D-induced mitochondrial dysfunction

As previously described, ACP@C-D can disintegrate in response to an acidic environment [34,35], so we studied the Ca^{2+} release from ACP@C-D in living cells using a Ca^{2+} fluorescent probe (Fluo-4AM). We first explored the intracellular Ca^{2+} concentration in 4T1 cells at different times after incubation with ACP@C-D (Fig. 3**A**). The green fluorescence in the cells gradually intensified as the incubation time increased, indicating a gradual increase in intracellular Ca^{2+}. Subsequently, we explored the concentration of Ca^{2+} in 4T1 cells after different treatments. As CLSM results show (Fig. 3**B**), the strongest green fluorescence was observed in the cell mitochondria after being treated with ACP@C-D, indicating a higher intracellular level of free Ca^{2+} in mitochondria. As shown in Figure S8, the mineralized cells had distinct absorption peaks at 563 cm^{-1} and 1033 cm^{-1}, which are characteristic peaks of PO_4^{3-}, indicating that the cells underwent calcium phosphate deposition with calcium phosphate mineral production. The intracellular Ca^{2+} content was also examined (Figure S9), and the results showed that compared with L02 cells, 4T1 cells had a higher concentration of Ca^{2+} and a higher degree of biomineralization, which was consistent with the results of previous studies. Concomitantly, the intracellular distribution of mitochondria was investigated through staining with TMRM (Tetramethylrhodamine, methyl ester, perchlorate) (Fig. 3**C**). Compared to other groups, the cells treated with ACP@C-D showed the weakest red fluorescence, indicating the lowest number of mitochondria and the most severe mitochondrial dysfunction. Mitochondrial dysfunction is often accompanied by ROS production, and we detected intracellular ROS levels after being treated with different

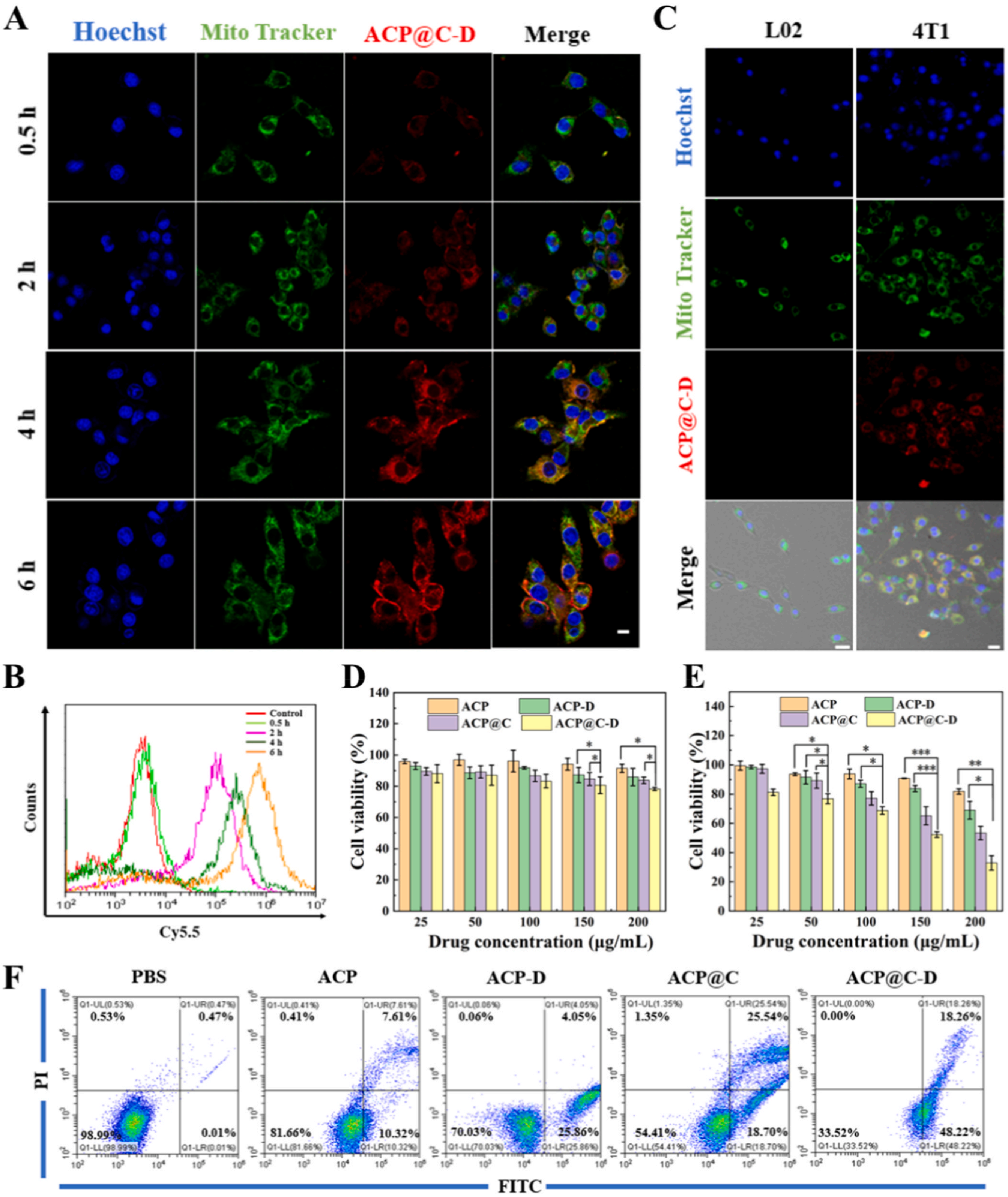

Fig. 2. **(A)** Confocal microscopy image analysis of 4T1 cells after incubation with ACP@C-D. Scale bar=20 μm. **(B)** Confocal microscopy image analysis of L02 cells and 4T1 cells after incubation with ACP@C-D. Blue fluorescence represents nuclei, green fluorescence represents mitochondria, and red fluorescence represents the fluorescence of Cy5.5. Scale bar=20 μm. **(C)** Flow cytometry analysis of ACP@C-D uptake of 4T1 cells at different times. Effects of different formulas on the viability of L02 **(D)** and 4T1 **(E)** cells. **(F)** Flow cytometry analysis of apoptosis of 4T1 after treatment with different formulas. The data are presented as mean±SD, n=3. Student's *t-test*, $^{*}p<0.05$, $^{**}p<0.01$, $^{***}p<0.001$, and $^{****}p<0.0001$.

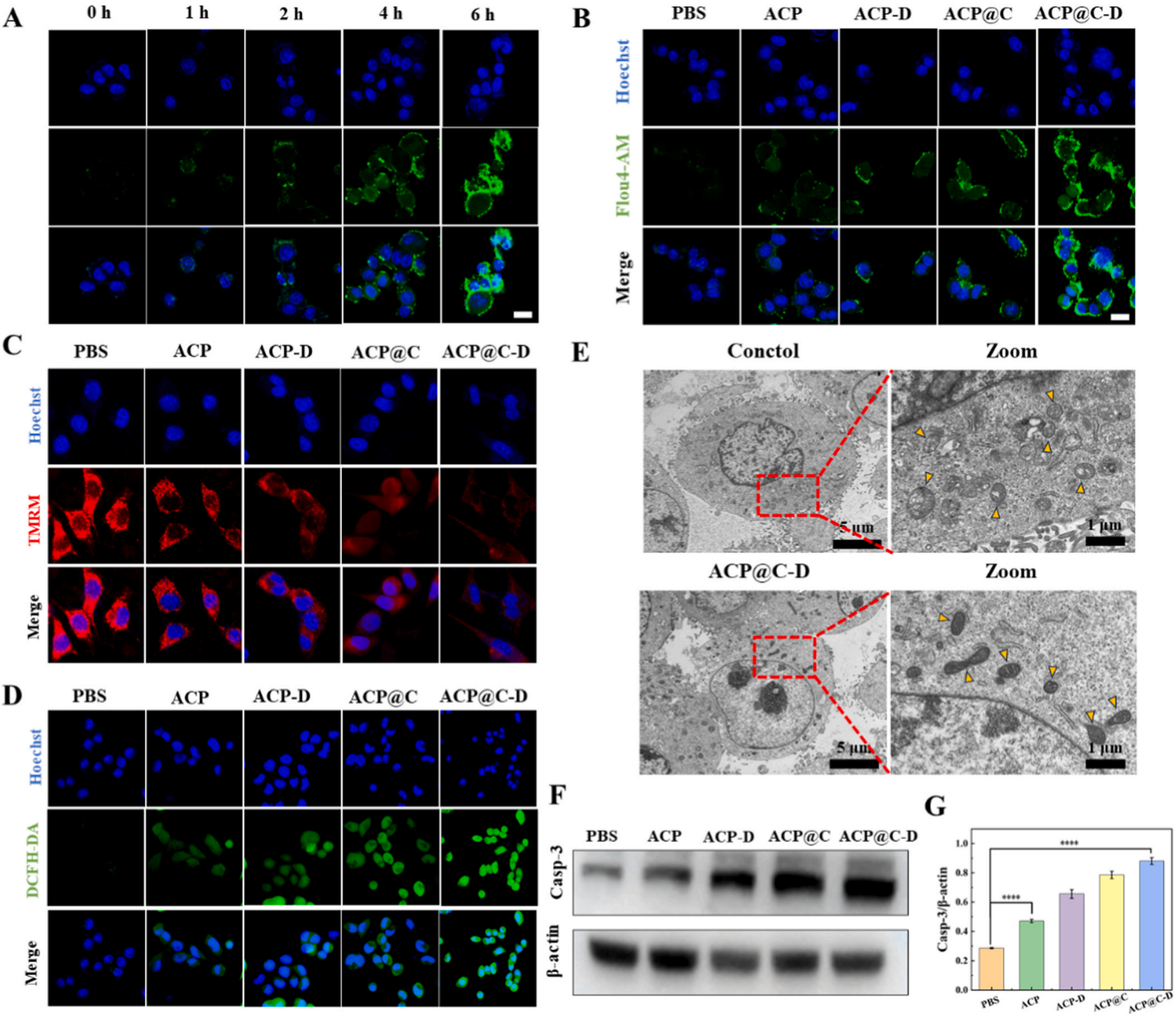

Fig. 3. Mitochondrial damage probed by ACP@C-D. (A) Fluorescence images of Ca levels in 4T1 cells at different times were detected by the Flou4-AM fluorescent probe after being treated with ACP@C-D. Scale bar=20 μm. **(B)** Fluorescence images of Ca levels in 4T1 cells were detected by the Flou4-AM fluorescent probe after being treated with different formulations. Scale bar=20 μm. **(C)** Confocal microscopy images of TMRM showing depolarization of mitochondrial membranes. Scale bar=20 μm. **(D)** ROS levels of cells were analyzed by DCFH-DA probe after different formulas acted on 4T1 cells. Scale bar=20 μm. **(E)** Biomicrograph microscopy images of 4T1 cells before and after 12 h of ACP@C-D treatment. **(F)** Results of Western blot analysis of caspase-3 (Casp-3) in 4T1 cells after the action of different formulations. **(G)** Gray analysis of protein blots. The data are presented as mean±SD, n=3. Student's *t-test*, $^{*}p<0.05$, $^{**}p<0.01$, $^{***}p<0.001$, and $^{****}p<0.0001$.

formulations using fluorescent probe DCFH-DA (Fig. 3**D**). Compared with negligible fluorescence in the PBS or ACP-D group and ACP@C group, cells treated with ACP@C-D exhibited the brightest green fluorescence, This is consistent with the results shown by flow cytometry (Figure S10). suggesting the most effective enhancement of intracellular oxidative stress.

Besides, the morphological changes in the mitochondria of the tumor cells in the different treatment groups were observed using Bio-TEM. As shown in Fig. 3**E**, ACP@C-D treatment resulted in maximal disruption of mitochondria, and high levels of mineral production within mitochondria were observed, whereas the mitochondria in 4T1 cells before treatment had normal morphology. Depolarization of the mitochondrial membrane is frequently coupled with Cyto-c spillover into the cytoplasm, which will upregulate caspase-3 expression. For this purpose, we examined the expression levels of proteins in the cells after various treatments through western blot (Fig. 3**F** and **G**). After treatment with different formulations, Caspase-3 in cells was activated in all the experimental groups, most obvious in the ACP@C-D group. Therefore, the significant mitochondrial dysfunction through the Ca^{2+} overload and mitochondrial biomineralization by ACP@C-D has been confirmed, which would facilitate the subsequent efficient apoptosis of cancer cells.

Biodistribution

Motivated by the cytotoxicity study in living cells, we intend to explore the tumor inhibitory effects of ACP@C-D *in vivo*. Before biomedical applications, we first explored the accumulation and retention capacity of ACP@C-D at the tumor location. As the fluorescence imaging shown in Fig. 4**A**, the fluorescence signal of individual Cy5.5-DNA was attenuated with time and there was almost no Cy5.5 fluorescence signal that can be observed at the tumor location within 24 h, indicating that the individual Cy5.5-DNA was quickly cleared by the

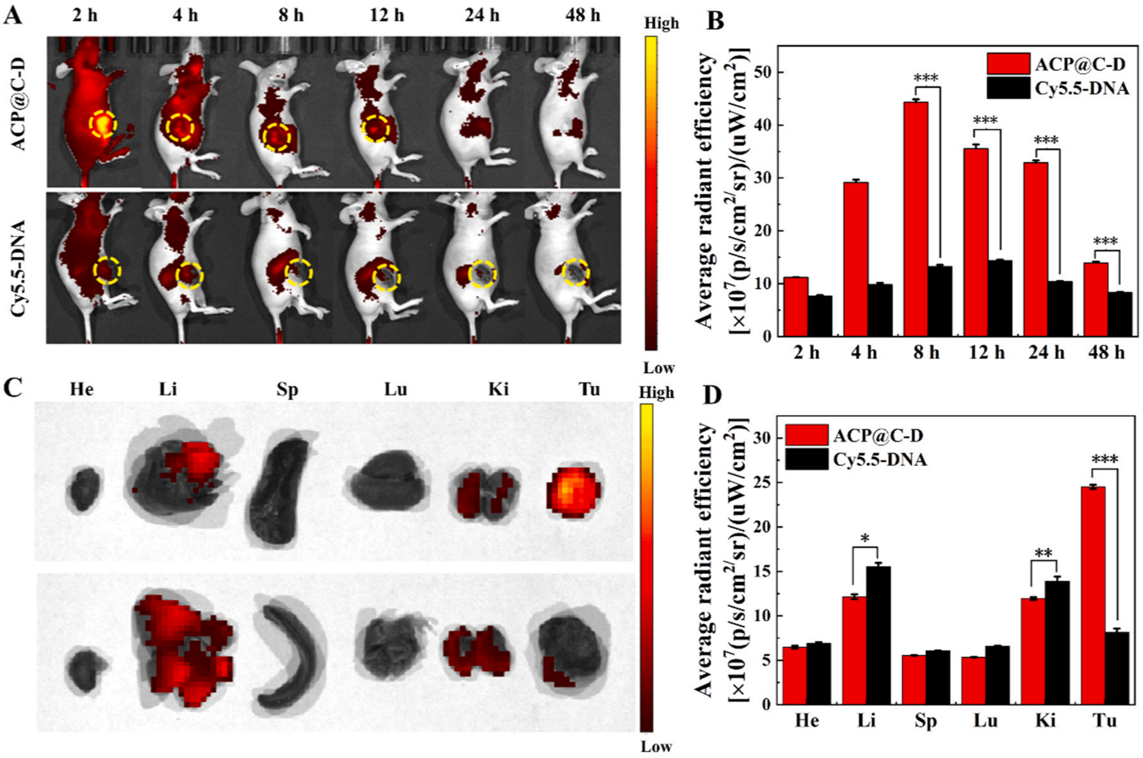

Fig. 4. Biodistribution and *in vivo* fluorescence imaging of 4T1 hormonal mice after intravenous injection. **(A)** Fluorescence images of 4T1 hormonal mice were observed after intravenous injection of ACP@C-D and free Cy5.5-DNA at 2, 4, 8, 12, 24, and 48 h, respectively. **(B)** The biodistribution of ACP@C-D and free Cy5.5-DNA in mice was determined using the corresponding tumor mean fluorescence intensity, respectively. Fluorescence images of tumors and organs at the end of the study (48 h after injection) **(C)** and semiquantitative analysis **(D)**. The data are presented as mean±SD, n=3. Student's *t-test*, $*p<0.05$, $**p<0.01$, $***p<0.001$, and $****p<0.0001$.

metabolic organ. However, the gradual accumulation of Cy5.5 fluorescence at the tumor site can be observed in periods of 2–8 h after ACP@C-D injection due to the enhanced permeability and retention (EPR) effect, which identified it as a promising fluorescence imaging agent for direct tracking tumor therapy. What is more, the semiquantitative analysis of fluorescence images at the tumor site showed that clear Cy5.5 fluorescence signals appeared at 2 h and peaked at 8 h after ACP@C-D injection (Fig. 4**B**), fluorescence can still be detected at the tumor location after 48 h. All mice were sacrificed and the fluorescence imaging of tumors and main organs was carried out at 48 h. Fluorescence images and semiquantitative analysis revealed that strong fluorescence can be noticed from the tumor in the ACP@C-D group, suggesting effective accumulation and high retention of ACP@C-D (Fig. 4**C** and **D**). remarkable fluorescence also can be found in the liver and kidney which could be attributed to the clearance of the endothelial reticulum system. In addition, hemolysis experiments were carried out on different concentrations of ACP@C-D (Figure S11), and the results proved that ACP@C-D has good biological safety.

In vivo synergistic therapy and biosafety

The enhanced tumor accumulation and favorable fluorescence imaging capacities of ACP@C-D enabled us to carry out anticancer assessments using a 4T1-tumor-bearing nude mouse model. 4T1-tumor-bearing nude mice with tumor volumes of around 100 mm^3 were randomly divided into five groups (n = 4 per group) and i.v. injected with ACP, ACP-D, ACP@C, ACP@C-D, or PBS as a control on days 1, 3, and 5 (Fig. 5**A**). To assess the antitumor efficacy, the body weight of mice and tumor volume were continuously surveyed. After two weeks of observation, the tumor grew rapidly and reached a volume 10-fold greater than the original volume in the saline group (Fig. 5**B**). Although ACP-D and ACP@C-D exhibited antitumor effects, the inhibitory effect is limited, reflecting that a single pathway of mitochondrial destruction could not produce satisfactory therapeutic efficacy. Distinctly, ACP@C-D resulted in a significantly reduced tumor burden with long-term tumor suppression than other groups, which is probably due to the presence of three distinct factors: (1) pH-responsive degradation of ACP effectively increases Ca^{2+} concentration to enhance Ca^{2+} overload; (2) CUR can inhibit the efflux of Ca^{2+}, which is further enhanced Ca^{2+} overload by increasing the concentration of endogenous Ca^{2+}; (3) The mitochondrial targeting of Cy5.5 enriched DNA aptamers in mitochondria, which can provide chelation sites for Ca^{2+} thereby promoting mitochondrial mineralization. No significant changes in body weight were observed in any of the groups during the treatment, demonstrating the safety of the treatment (Fig. 5**C**). The superior therapeutic efficacy was further intuitively displayed by comparing tumor weight (Fig. 5**E**) and tumor suppression rate (Fig. 5**F**) of dissected tumor tissue after 14 days of monitoring. Remarkably, the ACP@C-D showed a maximum inhibition ratio of 86.6 %, which was greater than that for those treated with ACP-D (34.3 %) or ACP@C (49.9 %). Photographs of mice at the end of the treatment cycle and digital photographs of isolated tumors (Fig. 5**D**) showed that the ACP@C-D group had the smallest tumors, sufficiently indicating the favorable tumor suppressive effect.

Histological observation of tumor sections was carried out at the end of treatment for pathological changes on the histological level (Fig. 5**G**). H&E staining revealed no significant damage to the cells in the saline group and ACP group; on the contrary, severe tissue destruction occurred in ACP-D and ACP@C. There was the most severe tissue damage after treatment with ACP@C-D. Likewise, the TUNEL assay showed that ACP@C-D resulted in the highest levels of apoptosis, as supported by the largest number of green fluorescent spots in visual fields. ACP@C-D can enhance mitochondrial dysfunction to activate the mitochondrial apoptotic pathway, which would upregulate the expression of Caspase-3. Following that, we investigated the expression of

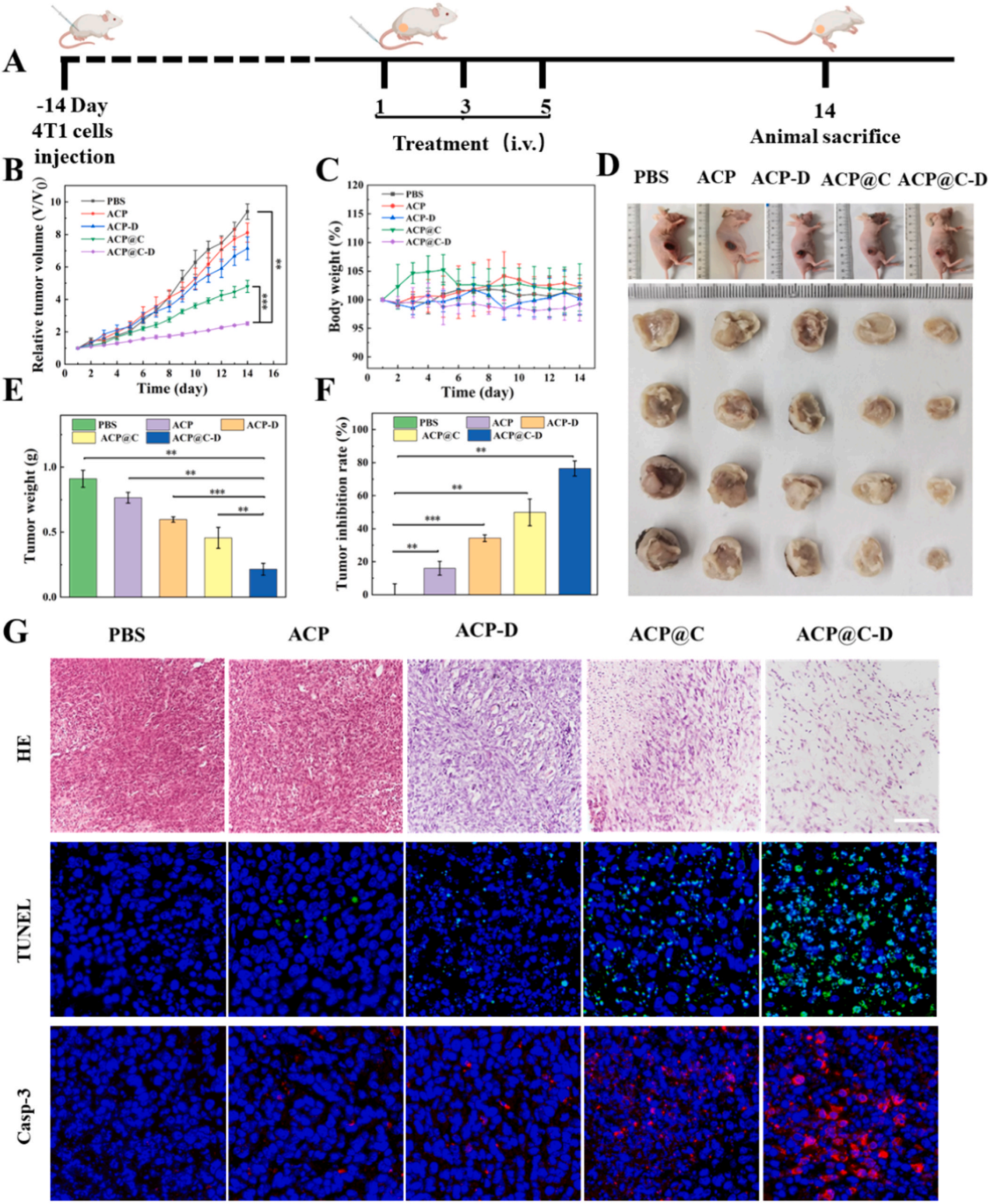

Fig. 5. *In vivo* synergistic therapy. **(A)** Schematic timeline of animal therapy. (B) Tumor volume growth curve of mice during the treatment cycle. **(C)** Body weight change curve of mice during the treatment cycle. **(D)** Comparison of photographs of mice and isolated tumors from different experimental groups at the end of the treatment cycle. **(E)** Tumor weight and **(F)** *in vivo* tumor suppression efficiency. **(G)** H&E staining (Scale bar=50 μm), TUNEL and Caspase-3 immunofluorescence staining (Scale bar=20 μm) of tumor tissues excised by different treatments. The number of groups: 1) PBS; 2) ACP; 3) ACP-D; 4) ACP@C; 5) ACP@C-D. The data are presented as mean±SD, n=5. Student's *t-test*, **p*<0.05, ***p*<0.01, ****p*<0.001, and *****p*<0.0001.

Caspase-3 through immunofluorescence. The immunofluorescence studies revealed that higher expression of Caspase-3 could be observed after being treated with ACP@C-D, in agreement with in western blot studies. Taken together, ACP@C-D can effectively inhibit cell proliferation and promote apoptosis in vivo through multilevel destruction of mitochondria, which has the potential to be an innovative Calcium-based nanomedicine for tumor therapy. After 14 days of treatment, the blood biochemical indexes and hematological parameters of mice were examined in the PBS and ACP@C-D treated groups (Figure S12). From the results of blood analysis, it was evident that the blood routine and blood biochemical indexes of mice in all the groups after different treatments were within the normal range. lastly, the biosafety of nanomodulators was finally examined by slaughtering mice for H&E staining of major organs. As shown in Figure S13, no pathological abnormalities were detected in the H&E staining of the major organs in each group, indicating that ACP@C-D and its mediated mitochondrial calcium mineralization therapy have good biosafety, which will help its future clinical application.

Conclusions

In summary, we successfully prepared nucleic acid-based Ca^{2+} nanomodulator ACP@C-D by a simple co-precipitation method and DNA adsorbed for use as a multi-therapeuticpromoted mitochondrial dysfunction-dominated cancer therapy through Ca^{2+} overload and mitochondrial mineralization. After systemic administration, this intracellular acidity-responsive Ca^{2+} nanomodulator could effectively enhance Ca^{2+} overload through the combination of the burst Ca^{2+} release and the inhibition of Ca^{2+} efflux. Specifically, Cy5.5-labeled DNA can efficiently aggregate in mitochondria to induce mitochondrial mineralization, which has never been reported before. Our results proved that ACP@C-D was an effective therapeutic formulation with enhanced anticancer efficacy, reduced systemic toxicity, and excellent fluorescence. We believe that this precisely designed multifunctional Ca^{2+} nanomodulator has great potential for use in mitochondriatargeted cancer therapy in clinical practice.

CRediT authorship contribution statement

Xuemei Li: Writing – original draft. **Huangxian Ju:** Writing – review & editing. **Geng Yang:** Data curation. **Weicai Wang:** Software. **Tingting Zhao:** Data curation. **He Yuan:** Methodology. **Weifang Gong:** Writing – original draft.

Declaration of Competing Interest

Weifang Gong, Xuemei Li and Huangxian Ju conceived the study, analyzed the data, and drafted the manuscript. Tingting Zhao, He Yuan, Geng Yang, and Weicai Wang assisted in data collection and study design. All authors read and approved the final manuscript and there are no conflicts to declare.

Data availability

No data was used for the research described in the article.

Acknowledgments

This work was supported by Taishan Scholars Program of Shandong Province (tsqn201812101) and the National Natural Science Foundation of China (21876074).

Appendix A. Supporting information

Supplementary data associated with this article can be found in the online version at doi:10.1016/j.nantod.2024.102465.

References

[1] T.L. Deshields, S. Wells-Di Gregorio, S.R. Flowers, K.E. Irwin, R. Nipp, L. Padgett, B. Zebrack, Nat. Rev. Drug. Discov. 71 (2021) 407–436.
[2] A. Mullard, Chin. J. Mod. Appl. Pharm. 19 (2020) 825–826.
[3] Z. Jing, Q. Du, X. Zhang, Chem. Eng. J. (2022) 446P443.
[4] M. Xu, C. Zhang, S. He, C. Xu, X. Wei, K. Pu, ACS Nano 17 (2023) 8183–8194.
[5] D. Yadav, M. Kwak, P.S. Chauhan, N. Puranik, P.C.W. Lee, J.O. Jin, Jin, Semin. Cancer Biol. 86 (2022) 909–922.
[6] T. Zhonghua, H. Mingchun, L. Jing, D.O. Pharmacy, J. Mod. Appl. Pharm. (2019) (750).
[7] M.M. Agwa, H. Elmotasem, R.I. Moustafa, A.S. Abdelsattar, M.S. Mohy-Eldin, M.M. G. Fouda, Int. J. Biol. Macromol. 253 (2023) 127460.
[8] Z. Liu, Y. Zhong, X. Zhou, X. Huang, J. Zhou, D. Huang, Y. Li, Z. Wang, B. Dong, H. Qiao, W. Chen, Biomaterials 277 (2021) 121118.
[9] T. Colombani, J. Sinoimeri, S.A. Bencherif, Cancer Immunol. Res. 8 (2020) B106.
[10] S.-F. Wang, L.-M. Tseng, H.-C. Lee, J. Biomed. Sci. 30 (2023) 61.
[11] T.T. Nguyen, S. Wei, T.H. Nguyen, Y. Jo, Y. Zhang, W. Park, K. Gariani, C.-M. Oh, H.H. Kim, K.-T. Ha, K.S. Park, R. Park, I.-K. Lee, M. Shong, R.H. Houtkooper, D. Ryu, Exp. Mol. Med. 55 (2023) 1595–1619.
[12] X. Sun, G. Ye, Y. Mai, Y. Shu, L. Wang, J. Zhang, Med. Res. Rev. 43 (2023) 855–871.
[13] C. Sandoval-Acuña, N. Torrealba, V. Tomkova, S.B. Jadhav, K. Blazkova, L. Merta, S. Lettlova, M.K. Adamcová, D. Rosel, J. Brábek, J. Neuzil, J. Stursa, L. Werner, J. Truksa, Cancer Res. 81 (2021) 2289–2303.
[14] R.X. Zhang, L.Y. Li, J. Li, Z. Xu, A.Z. Abbasi, L. Lin, M.A. Amini, W.Y. Weng, Y. Sun, A.M. Rauth, X.Y. Wu, Adv. Funct. Mater. 27 (2017) 1700804.
[15] M. Li, X. Luo, S. Lei, Y. Liu, H. Guo, Y. Zhang, Y. Pan, K. Chen, J. Lin, P. Huang, Adv. Mater. 35 (2023) 2301099.
[16] Y. Elkis, M. Cohen, E. Yaffe, S. Satmary-Tusk, T. Feldman, E. Hikri, A. Nyska, A. Feiglin, Y. Ofran, S. Shpungin, U. Nir, Nat. Commun. 8 (2017) 940.
[17] Y. Kang, L. Xu, J. Dong, Y. Huang, X. Yuan, R. Li, L. Chen, Z. Wang, X. Ji, Chem. Rev. 481 (2023) 215050.
[18] R.A. Hutto, C.M. Bisbach, F. Abbas, D.C. Brock, W.M. Cleghorn, E.D. Parker, B. H. Bauer, W. Ge, F. Vinberg, J.B. Hurley, S.E. Brockerhoff, Cell. Death Differ. 27 (2020) 1067–1085.
[19] Q. Sun, B. Liu, Z. Wang, L. Feng, R. Zhao, S. Dong, Y. Dong, L. Zhong, S. Gai, P. Yang, Chem. Eng. J. 425 (2021) 131485.
[20] Y. Feng, R. Qin, L. Xu, X. Ma, D. Ding, S. Li, L. Chen, Y. Liu, W. Sun, H. Chen, Theranostics 12 (2022) 734–746.
[21] C. Wang, T. Li, Z. Wang, Y. Li, Y. Liu, M. Xu, Z. Zhang, Y. Deng, L. Cai, C. Zhang, C. Li, J. Nanobiotechnol. 21 (2023) 465.
[22] M. Marchesini, A. Gherli, A. Montanaro, S. Kitara, C. Sorrentino, L. Pagliaro, A.-M. Lund Winter, C. Rompietti, D. Stilli, F. Rizzi, K. Stegmaier, P. Sportoletti, W. Dalby-Brown, G. Roti, Targeting the activating mutations of NOTCH1 in T-cell lymphoblastic leukemia with a new SERCA inhibitor CAD204520, Blood 134 (2019) 407.
[23] M. Fan, J. Zhang, C.-W. Tsai, B.J. Orlando, M. Rodriguez, Y. Xu, M. Liao, M.-F. Tsai, L. Feng, Nature 582 (2020) 129–133.
[24] I. Parkkinen, A. Their, M.Y. Asghar, S. Sree, E. Jokitalo, M. Airavaara, Pharmacol. Rev. 75 (2023) 959–978.
[25] P. Zheng, B. Ding, G. Zhu, C. Li, J. Lin, Angew. Chem. Int. Ed. 61 (2022) e202204904.
[26] X. Wang, X. Ge, X. Guan, J. Ouyang, N. Na, Chem. Sci. 14 (2023) 11532–11545.
[27] P. Zheng, B. Ding, R. Shi, Z. Jiang, W. Xu, G. Li, J. Ding, X. Chen, Adv. Mater. 33 (2021) 2007426.
[28] X. Wang, Y. Li, F. Jia, X. Cui, Z. Pan, Y. Wu, J. Nanobiotechnol. 20 (2022) 225.
[29] W. Wang, X. Liu, X. Zheng, H.J. Jin, X. Li, Adv. Healthc. Mater. 9 (2020) 2001117.
[30] R. Zhao, B. Wang, X. Yang, Y. Xiao, X. Wang, C. Shao, R. Tang, Angew. Chem. Int. Ed. 55 (2016) 5225–5229.
[31] N. Tang, H. Li, L. Zhang, X. Zhang, Y. Chen, H. Shou, S. Feng, X. Chen, Y. Luo, R. Tang, B. Wang, Chem. Int. Ed. 60 (2021) 6189.
[32] Z. Jiang, Y. Liu, R. Shi, X. Feng, W. Xu, X. Zhuang, J. Ding, X. Chen, Adv. Mater. 34 (2022) 2110094.
[33] Y. Liu, Z. Jiang, S. Tong, Y. Sun, Y. Zhang, J. Zhang, D. Zhao, Y. Su, J. Ding, X. Chen, Adv. Mater. 35 (2023) 2203291.
[34] B. Xie, H. Zhao, Y.-F. Ding, Z. Wang, Y. Wang, C. Gao, R. Wang, J. Control. Release 357 (2023) 572–579.
[35] S. Kim, L. Palanikumar, H. Choi, M.T. Jeena, C. Kim, J.-H. Ryu, Chem. Sci. 9 (2018) 2474–2479.
[36] T.S. Luongo, J.P. Lambert, P. Gross, M. Nwokedi, A.A. Lombardi, S. Shanmughapriya, A.C. Carpenter, D. Kolmetzky, E. Gao, J.H. van Berlo, E.J. Tsai, J.D. Molkentin, X. Chen, M. Madesh, S.R. Houser, J.W. Elrod, Nature 545 (2017) 93–97.
[37] E. Murphy, C. Steenbergen, Annu. Rev. Physiol. 83 (2021) 107–126.
[38] X. Chang, X. Tang, J. Liu, Z. Zhu, W. Mu, W. Tang, Y. Zhang, X. Chen, Adv. Funct. Mater. 33 (2023) 2303596.
[39] E. Duffy, J. Florek, S. Colon, A.E. Gerdon, Anal. Chim. Acta 1110 (2020) 115–121.
[40] R. Lai, G. Li, Q. Cui, J. Am. Chem. Soc. 146 (2024) 7628–7639.
[41] S. Wu, M. Zhang, J. Song, S. Weber, X. Liu, C. Fan, Y. Wu, ACS Nano 15 (2021) 1555–1565.
[42] X. Guo, W. Li, H. Wang, Y.-Y. Fan, H. Wang, X. Gao, B. Niu, X. Gong, J. Non-Cryst. Solids 500 (2018) 317–325.
[43] D. Athanasiadou, K.M.M. Carneiro, Nat. Rev. Chem. 5 (2021) 93–108.
[44] X. Liu, X. Jing, P. Liu, M. Pan, Z. Liu, X. Dai, J. Lin, Q. Li, F. Wang, S. Yang, L. Wang, C. Fan, Chem 6 (2020) 472–485.

[45] S. Xie, W. Sun, T. Fu, X. Liu, P. Chen, L. Qiu, F. Qu, W. Tan, J. Am. Chem. Soc. 145 (2023) 7677–7691.

[46] G. Li, Y. Chen, L. Zhang, M. Zhang, S. Li, L. Li, T. Wang, C. Wang, Nano-Micro Lett. 10 (2017) 7.

[47] C.H. Liu, G.J. Chern, F.F. Hsu, K.W. Huang, Y.C. Sung, H.C. Huang, J.T. Qiu, S. K. Wang, C.C. Lin, C.H. Wu, H.C. Wu, J.Y. Liu, Y. Chen, Hepatology 67 (2018).